Fermi blockade of the strong electron-phonon interaction in optimally doped high temperature superconductors

Andrey Mishchenko (✉ mishchenko@riken.jp)
RIKEN Center for Emergent Matter Science

Naoto Nagaosa
RIKEN Center for Emergent Matter Science

Nikolay Prokof'ev
University of Massachusetts Amherst

Igor Tupitsyn
University of Massachusetts Amherst

Research Article

Fermi blockade of the strong electron-phonon interaction in optimally doped high temperature superconductors.

Andrey S. Mishchenko[*,1], Igor S. Tupitsyn[2], Naoto Nagaosa[1,3], and Nikolay Prokof'ev[2]

[1]RIKEN Center for Emergent Matter Science (CEMS), Wako, Saitama 351-0198, Japan

[2]Department of Physics, University of Massachusetts, Amherst, MA 01003, USA

[3]Department of Applied Physics, The University of Tokyo 7-3-1 Hongo, Bunkyo-ku, Tokyo 113-8656, Japan

We study how manifestations of strong electron-phonon interaction (EPI) depend on the carrier concentration by solving the two-dimensional Holstein model for the spin-polarized fermions using an approximation free bold-line diagrammatic Monte Carlo (BDMC) method. We show that the strong EPI, obviously present at very small Fermion concentration, is masked by the Fermi blockade effects and Migdal's theorem to the extent that it manifests itself as moderate one at large carriers densities. Suppression of strong EPI fingerprints is in agreement with experimental observations in doped high temperature superconductors.

Discussions on the role of the EPI in the physics of cuprate compounds with high superconducting transition temperatures (high T_c) have been going for decades [1, 2, 3, 4, 5, 6] without resulting in a consensus opinion. While the role of EPI in superconductivity is still under debate, its strong manifestations were clearly observed in numerous other phenomena in high T_c materials [5, 6, 7, 8, 9, 10, 11, 12, 13, 14]. The apparent puzzle is that strong EPI effects seen in spectroscopic data of undoped and weakly doped compounds become much less pronounced with hole doping [15, 16, 17, 18, 19, 20, 21]. Hence, having a clear picture of how the EPI effects change with the carrier concentration is of seminal importance for understanding the nature of unconventional superconductors where rigorous studies are hindered by the complexity of many-body fermion problem. Accurate results on the EPI in many-fermion systems may provide the way to reconcile the observed fingerprints of the strong EPI in the underdoped regime with successful descriptions of the strongly doped high T_c materials by models based on direct electron-electron interactions alone.

More generally, it is a long standing fundamental problem to reveal how the Migdal's theorem [22, 23] emerges at the large fermion concentration and eliminates the need for vertex corrections even for strong EPI, provided the Fermi-liquid state remains stable. Violations of the Migdal theorem in high temperature superconductors were discussed for decades [24]. Most studies [25, 26] only evaluate the lowest order corrections whereas our goal is to have a complete picture where all approximations, order-by-order, are compared to the exact answer as the fermion concentration approaches zero. The crossover between the two regimes is expected to take place at $\omega_{\mathrm{ph}} \sim \varepsilon_F$, where ω_{ph} is the phonon frequency and ε_F is the Fermi energy, and it can be addressed by the approximation free diagrammatic Monte Carlo methods [27, 28, 8, 29].

To this end, we consider a spin polarized (SP) two-dimensional (2D) lattice system in order to avoid system instabilities that would be triggered by the strong EPI in continuous and spin-balanced systems, such as structural transitions or a singlet on-site bipolaron formation at $\lambda \approx 0.5$ (in 2D) [30] with the concomitant superconducting state. An essential feature of the SP Holstein model resembling that of the $t-J$ model near half-filling [31, 32] (which is prototypical for description of high T_c superconductors) is that in both cases one can only create one hole per site. Strong repulsive electron-electron interactions obviously play a key role close to half-filling. However, our study is focused on the small density regime where Hubbard-type interactions can be treated perturbatively (after strong on-site repulsion is replaced with an exact solution of the two-body scattering problem) and result only in weak renormalization of electron properties. When the electron-phonon coupling is strong, repulsive electron-electron interactions are required for system stabilization against the bi-polaron instability, but otherwise their effects remain perturbative. This is precisely the situation that we are modeling at the microscopic level in our work.

1. Exact numeric approach

In this work we employ the BDMC technique developed for many-body systems with EPI in Ref. [29]. For the same system parameters the determinant Monte Carlo [33, 34, 35] method would suffer from a severe sign problem. The dynamical mean-filed method (DMFT) [36, 37], would be inadequate because the EPI self-energy is strongly momentum dependent at low carrier concentration [29], in violation of the key DMFT assumption. The BDMC technique is based on the expansion of irreducible free-energy Feynman diagrams in terms of exact electron, G, and bare, $D^{(0)}$, phonon propagators and is free from the above limitations. We consider phonon propagators $D^{(0)}$ as exact, fully renormalized/dressed functions as if they are already the result of an accurate ab-initio treatment [38, 39]. Thus, we omit all diagrams that can be interpreted as the phonon proper self-energy insertion; accounting for phonon renormalization would have no significant effect on our results because we focus on the small carrier concentration limit. In more detail, see Ref. [29], the electron self-energy $\Sigma^{(m)}$ is expanded into the series of irreducible skeleton graphs up to the largest order m defined by the number of $D^{(0)}$ propagators, with self-consistency implemented by a feedback loop involving the solution of the algebraic Dyson equation, $[G(\mathbf{k}, \omega_\ell)]^{-1} = [\mathbf{G^{(0)}}(\mathbf{k}, \omega_\ell)]^{-1} - \mathbf{\Sigma^{(m)}}(\mathbf{k}, \omega_\ell)$, in momentum, $\mathbf{k}$, and Matsubara frequency, $\omega_\ell = 2\pi T(\ell + 1/2)$, representation ($\ell$ is an integer).

2. Model

The 2D Holstein model on a square lattice reads:

$$(1) \qquad H = -t \sum_{<i,j>} c_i^\dagger c_j + \omega_{\mathrm{ph}} \sum_i b_i^\dagger b_i + g \sum_i c_i^\dagger c_i \left(b_i^\dagger + b_i \right),$$

where $c_i^\dagger / b_i^\dagger$ are standard notations for electron/phonon creation operators, t is the nearest neighbor hopping amplitude, $\omega_{\mathrm{ph}} = 0.5t$ is the energy of the local optical mode, and g is the EPI coupling. The electron gas is spin-polarized and, hence, any site can be occupied by no more than one electron. It is standard to characterize the strength of the EPI by a dimensionless coupling constant $\lambda = g^2/(4\omega_{\mathrm{ph}}t)$. The

89 lattice constant a, amplitude t, and Planck's constant $\hbar$ are used to set units of
90 length, energy, and time, respectively. In this study we chose $\lambda = 1.07$ beyond
91 the crossover from weak- to strong-coupling regimes for single polarons and the
92 threshold for the singlet bipolaron formation. For convenient systematic error-
93 free handling of the data in momentum space we perform simulations for finite
94 systems with 16×16 sites, large enough to reproduce the infinite system results
95 with high accuracy (see Supplemental Material [40]). The temperature is set to
96 $T = t/20$, which is an order of magnitude smaller than all energy scales of the
97 model parameters. In the zero-density limit an alternative exact (numerically)
98 diagrammatic Monte Carlo (DMC) approach for single polarons [27, 28] provides
99 reference values for the ground state energy, $E_1 = -4.891$, and the quasiparticle
100 (QP) residue, $Z_1 = 0.238$.

3. Results

102 Our main results are presented in Figs. 1, 2, and 3. Figure 1 shows the de-
103 pendence of the QP residue on the adiabaticity ratio $\gamma = \varepsilon_F/\omega_{\mathrm{ph}}$. One can see
104 in Fig. 1 that at large $\gamma \geq 3$ the Migdal's theorem ensures that vertex corrections
105 are small and the lowest-order $m = 1$ skeleton diagram for self-energy (also known,
106 depending on the context, as the non-crossing, the self-consistent Born, and the
107 Eliashberg approximations) well describes the EPI renormalization even at strong
108 coupling. In contrast, for smaller values of γ one has to account for high-order
109 vertex corrections; up to order $m = 7$ at $\gamma = 1$ and all the way to $m > 20$ for $\gamma \to 0$
110 with extrapolation to the infinite diagram-order limit. An immediate conclusion is
111 that EPI strongly suppresses the QP residue to values smaller that 0.5 (indicative
112 of strong coupling) only at a rather small filling factor when $\gamma < 1$.

113 In Fig. 2(a) we further quantify the role of vertex corrections at low and high
114 carrier density (or occupation number per site), δ, in both adiabatic and anti-
115 adiabatic regimes. Vertex corrections become important at $\gamma < 3$, and at low
116 values of γ and δ it is not sufficient to take into account just $m = 2$, or even $m = 3$
117 contributions; in this parameter regime the convergence is reached only for $m \geq 16$
118 in the skeleton expansion, see Fig. 2(a)). Figure 2(b) is complementary to Fig. 1
119 by presenting the data as a function of the carrier concentration δ instead of γ.
120 Signatures of strong EPI are observed only at $\delta < 0.1$ that roughly corresponds to
121 $\gamma \approx 1$, which can be interpreted as the "Fermi blockade" of EPI manifestations at
122 large concentration by the Pauli exclusion principle.

123 The key conclusion that clear signatures of strong EPI are limited to small doping
124 is consistent with experimental findings for high T_c superconductors [15, 19, 20, 21].
125 It is not restricted to specific model features or choice of parameters. For example,
126 smaller values of the phonon frequency lead to sharper crossover between the weak
127 and strong coupling regimes for single Holstein polarons (see Supplemental Material
128 [40]). Therefore, the crossover presented in Figs. 1 and 2 will be more pronounced
129 for smaller phonon frequencies. Besides, similar results are obtained for the spin-
130 balanced case when the bi-polaron instability is prevented by adding an on-site
131 Hubbard repulsion, $H_{\mathrm{Hub}} = \sum_i U n_{i\uparrow} n_{i\downarrow}$ with $n_{i\sigma} = c_{i\sigma}^\dagger c_{i\sigma}$, to the Hamiltonian
132 (see Supplemental Material [40]). [The corresponding simulations are far more
133 demanding.]

134 One evidence for Fermi blockade of the EPI with doping comes from angle re-
135 solved photoemission experiments [15]. It was shown that the ratio $v_{\mathrm{high}}/v_{\mathrm{low}}$

136 between the phase velocities of the dispersion relation above and below the De-
137 bye frequency, decreases with doping. Our simulations reveal a similar trend, see
138 Fig. 3. The QP dispersion relation $\omega(\mathbf{k})$ was obtained from the energy of the lowest
139 peak in the Lehmann spectral function, see Fig. 4, extracted from the imaginary
140 time Matsubara Green function $G(\tau)$ by the stochastic optimization with consistent
141 constraints method of analytic continuation [28, 41].

142   Calculations of the frequency dependent optical conductivity [19] and angle re-
143 solved photoemission spectra [21] in the low-concentration limit (one hole) of the
144 $t - J$-Holstein model revealed that the experimental dependence of both quantities
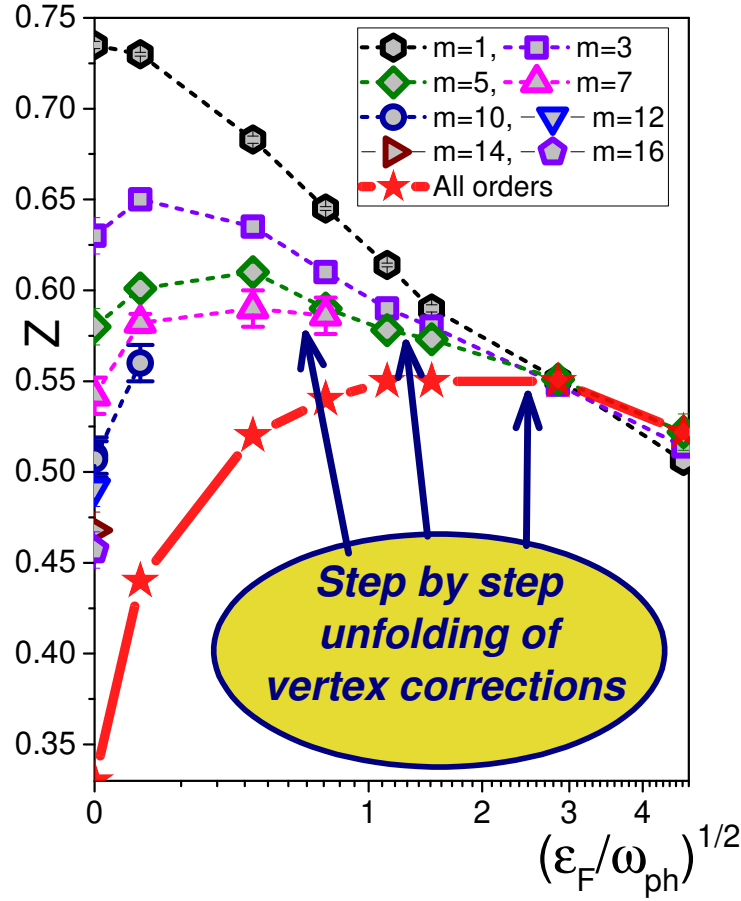

FIGURE 1. Quasi-particle residue at the Fermi (FS) as a function of ratio between the Fermi energy and phonon frequency without ($m = 1$) and with vertex corrections ($m > 1$). Symbols and dashed lines represent data obtained by skeleton expansions truncated at some finite order m. The solid red line with stars is obtained by extrapolation to the infinite diagram-order limit $m \to \infty$. The errorbars, if not visible, are smaller than the symbol sizes.
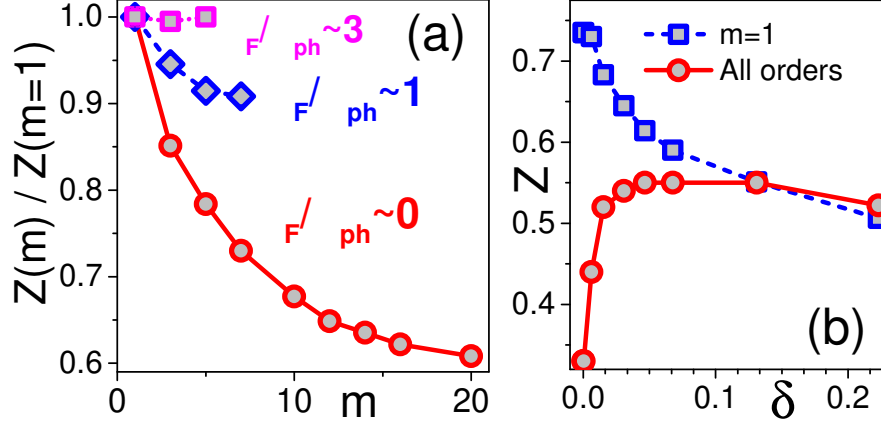
Figure 2. (a) Ratio between the quasi-particle residue deduced from diagrams up to order m and $m = 1$ (neglecting vertex corrections). Circles, diamonds, and squares stand for $\gamma \to 0$ ($\delta = 3.8 \times 10^{-4}$), $\gamma = 0.71$ ($\delta = 0.0308$), and $\gamma = 2.86$ ($\delta = 0.131$), respectively. (b) Quasi-particle residue at the Fermi (FS) as a function of carrier concentration δ (circles, infinite diagram-order limit) in comparison with the $m = 1$ result (squares), see also Fig. 1.

145 on δ can be reproduced theoretically if one introduces effective EPI coupling con-
146 stant $\lambda^e(\delta)$ that decreases with doping. It can be deduced from the photoemission
147 spectra using scaling relation [21]

$$
(2) \qquad \lambda^e = \sqrt{\frac{v_{\text{high}} - v_{\text{low}}}{20 v_{\text{low}}}} \,,
$$

148 derived from nonperturbative calculations for the $t - J$-Holstein model, where v_{low}
149 (v_{high}) is the velocity above (below) the kink energy ω_{ph}.
150   Kinks in the photoemission spectra are experimentally observed on the side of the
151 Fermi surface where the electron (or hole) bandwidth exceeds the phonon frequency.
152 Additional spectral features (rather typical in the small density limit when the
153 Fermi energy is smaller than ω_{ph}) are associated with the phonon sidebands [42].
154 Approximation free studies of the kink phenomenon show [21] that, in general, the
155 kink coexists with the phonon sidebands and only poor resolution or additional
156 damping mechanisms smear out the sidebands [43, 21] leading to a prototypical
157 picture of a sudden velocity change. Note, at least one phonon sideband, seen
158 as the doubling of the spectral peak around the kink energy, is present in most
159 theoretical calculations [7, 43, 44, 21] and this is precisely what we see in Fig. 3 at
160 $\omega/\omega_{\text{ph}} \approx 1$ and small momentum $k < 1$.
161   We compare $\lambda^e(\delta)$ deduced from experimental data of Ref. [21] with our theoret-
162 ical analysis in the inset of Fig. 3, dashed versus solid line. To have a meaningful
163 quantitative comparison we also need to account for the difference between the
164 non-degenerate spectrum of the spin-polarized Holstein model and fourfold degen-
165 erate ground state minimum of the experimental system. To this end we re-plot
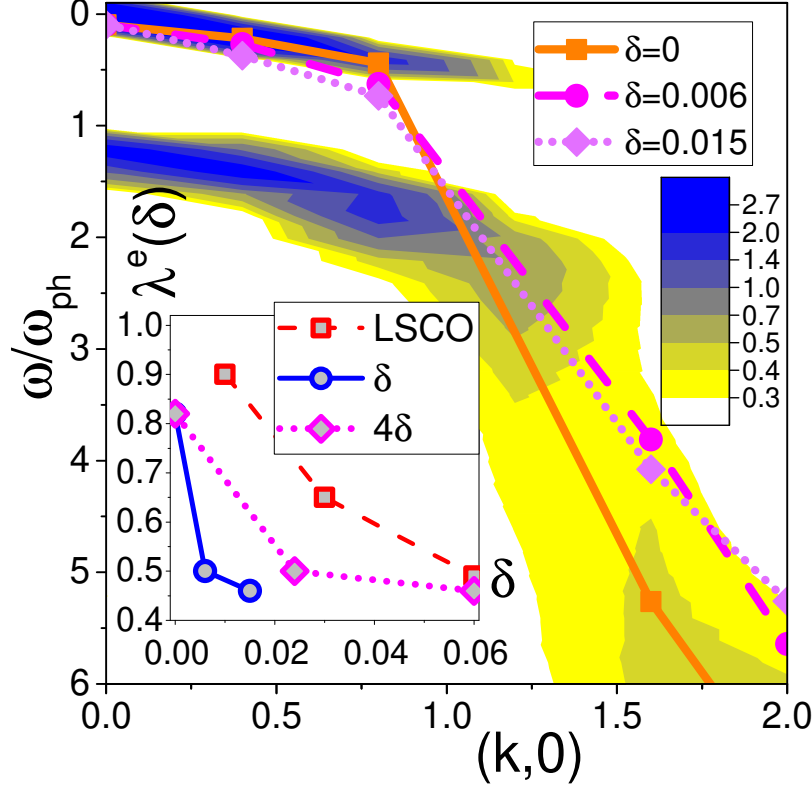
FIGURE 3. Contour plot of the spectral function intensity at $\delta = 3.8 \times 10^{-4}$ with blue/yellow color used for the large/small intensity. Symbols connected with lines mark locations of the spectral density maxima, see also Fig. 4, for: $\delta = 3.8 \times 10^{-4}$ (squares connected by the solid line), $\delta \approx 0.006$ (circles connected by the dashed line), and $\delta \approx 0.015$ (diamonds connected by the dotted line). In the inset we present the effective coupling constant λ^e deduced from the scaling relation (2) using experimental data for LSCO [21] (squares connected by a dashed line) and locations of theoretical spectral density maxima in Fig. 4 (circles connected by a solid line). We also re-plot the same theoretical data by using 4δ for the horizontal axis (diamonds connected by a dotted line). Spectral densities were computed for self-energies evaluated up to order $m = 16$ ($\delta = 3.8 \times 10^{-4}$), $m = 7$ ($\delta = 0.006$), and $m = 5$ ($\delta = 0.015$). These expansion orders are enough to have converged results for the corresponding carrier density (see Supplemental Material [40], Table I). Prepared by OriginPro 2016, http://OriginLab.com.

theoretical data using 4δ for the carrier concentration (dotted line). We observe semi-quantitative agreement between the theory and experiment despite a number of significant differences between the real systems and SP Holstein model at the microscopic level.

4. Discussion

The violation of Migdal's theorem for $T = 0$ is apparent in Fig. 1 for all filling factors except the two largest ones. At the lowest carrier concentrations the condition $\varepsilon_F \gg T$ does not hold any more, but this fact is barely relevant for the discussion because the theorem is severely violated well before that, at $\varepsilon_F \sim \omega_{\mathrm{ph}} \gg T$. Thus, our finite temperature results are still valid for interpretation of the EPI suppression in high T_c materials, which is observed from low to room temperatures [15, 19, 20, 21].

The suppression of the EPI effects considered here is not related to the weakening of the EPI due to screening at larger doping, see e.g. [47, 48], because we do not change the coupling strength λ and the phonon propagator with doping. In addition to the discussed EPI mechanism of how electronic properties are renormalized in cuprates, one has to consider electron-electron interactions and the emergent strong spin-fluctuations, see, e.g. discussions in Refs. [49, 50]. However, these additional important considerations are most relevant at large electron concentration close to half-filling, while the doping dependence discussed in this work takes place in the opposite limit.

5. Conclusions

We obtained approximation-free results for the concentration dependence of the quasiparticle residue Z and kink caused by the strong electron-phonon interaction in the spin-polarized two-dimensional Holstein model on the square lattice. We demonstrated that clear signatures of strong electron-phonon coupling at small carrier concentration are quickly suppressed for Fermi energies exceeding the phonon frequency. Our results provide detailed account for importance of high-order vertex corrections across the adiabatic crossover and demonstrate that Fermi blockade of the electron-phonon interaction and irrelevance of vertex corrections both proceed in agreement with the Migdal's theorem. This picture explains experimental results reporting radical weakening of the electron-phonon coupling effects in lightly doped high temperature superconductors. The Fermi blockade phenomenon is not restricted to high temperature superconductors and has to be observed in any material showing strong electron-phonon effects at small electron concentration.

6. Methods

All data for the QP residues at the FS, also denoted as Z_{FS}, were deduced from the Fermi-liquid relation, $Z_{FS} = [1 + d]^{-1}$, with $d = \partial Re[\Sigma(k_F, \omega)]/\partial \omega|_{\omega=0}$. In the low-temperature limit, the self-energy derivative at zero frequency is accurately obtained from the ratio $-Im[\Sigma(k_F, \ell)]/\omega_\ell$ at the lowest Matsubara frequencies. As expected, this procedure works perfectly at large carrier concentration. However, in the zero density limit the Fermi surface shrinks to a point at zero momentum, and the entire protocol becomes questionable. Spectral density offers an alternative way of computing the QP residue from the integrated weight of the lowest frequency peak (we denote it as Z_{GF}), see Fig. 4. Somewhat surprisingly, we find that even in the zero-density limit both procedures produce consistent results at any expansion order m, see inset in Fig. 4. At small, but finite concentration $\delta = 0.01526$ (or $\gamma = 0.334$), with Fermi-momentum $k_F \approx \pi/8$ the agreement is even more precise: at order $m = 5$ we find that $Z_{FS} = 0.605$ and $Z_{GF}(k_F = \pi/8) = 0.611$.

As already mentioned in connection with Figs. 1 and Fig. 2(a), at small doping the skeleton expansion needs to go beyond $m = 16$ in order to obtain correct results for the QP residue. However, both Z and the polaron energy E at the FS accurately follow an empirical scaling relation, $a + b/\sqrt{m}$, at any carrier concentration δ, see Fig. 5. This allows us to perform an extrapolation to the infinite-order limit to eliminate the remaining systematic error as shown in Figs. 1-2. The extrapolation procedure is validated by an excellent agreement between the BDMC result for the ground state energy of single-polarons, $E(m \to \infty) = -4.89$ and the DMC benchmark $E_1 = -4.891$. The single polaron zero temperature residue $Z_1 = 0.238$ is renormalized to $Z_1(\beta = 20) \approx 0.31$ due to finite temperature projection of the low energy self-trapping states [45, 46] (see Supplemental Material [40]) which is also consistent with extrapolated value $Z(m \to \infty) \approx 0.33$.
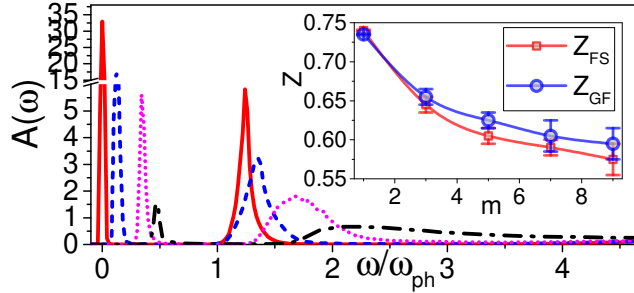

FIGURE 4. Spectral functions $A(\omega)$ at different momenta for $\delta = 3.8 \times 10^{-4}$ from $m = 16$ simulations: $q = (0, 0)$ (red solid line), $q = (\pi/8, 0)$ (blue dashed line), $q = (2\pi/8, 0)$ (magenta dotted line), and $q = (3\pi/8, 0)$ (black dash-dotted line). Energy zero was set at the value of the QP dispersion relation at $q = 0$. Inset: Order-by-order comparison between the two alternative procedures for computing the quasi-particle residue at $q = 0$: (i) using standard Fermi liquid relations at the Fermi surface, Z_{FS}, and (ii) from the lowest-frequency peak in the spectral function, Z_{GF}.
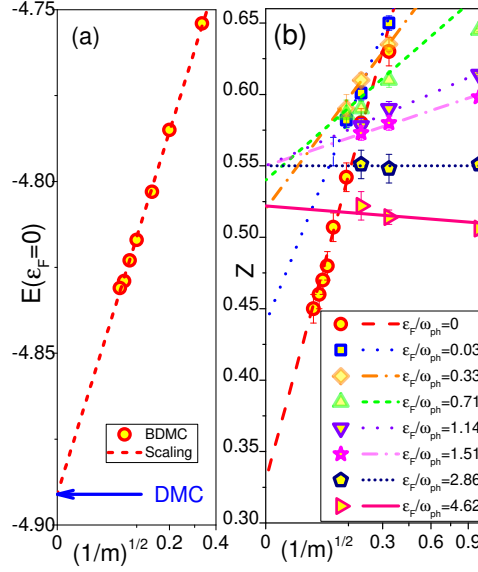
FIGURE 5. Finite expansion-order corrections to the polaron energy (a) and QP residue (b) revealing linear scaling with $m^{-1/2}$. (a) BDMC data (circles) and the scaling law $a + b/\sqrt{m}$ (dashed line) for the ground state energy at $\delta = 3.8 \times 10^{-4}$. The DMC result at $\delta = 0$ is shown by the blue arrow. (b) BDMC data (symbols) and the scaling laws $a + b/\sqrt{m}$ (lines) for the quasi-particle residue.

7. Data availability

The data presented are available from the corresponding authors upon reasonable request

References

[1] Anderson, P. W. *The Theory of Superconductivity in the High-T_c Cuprate Superconductors.* (University Press, Princeton, 1997)

[2] Alexandrov, A. S. Bipolaron anisotropic flat bands, Hall mobility edge, and metal-semiconductor duality of overdoped high-T_c oxides. *Phys. Rev. B.* **53**, 2863–2869 (1996).

[3] Anderson, P. W. Is There Glue in Cuprate Superconductors? *Science.* **316**, 1705–1707 (2007).

[4] Alexandrov, A. S. Bose-Einstein condensation of strongly correlated electrons and phonons in cuprate superconductors. *Journal of Physics: Condensed Matter.* **19**, 125216 (2007).

[5] Gunnarsson, O & Rösch, O. Interplay between electron-phonon and Coulomb interactions in cuprates. *Journal of Physics: Condensed Matter.* **20**, 043201 (2008).

[6] Mishchenko, A. S. Electron-phonon coupling in underdoped high-temperature superconductors. *Physics-Uspekhi.* **52**, 1193-1212 (2009).

[7] Rösch, O. & Gunnarsson, O. Electron-Phonon Interaction in the $t-J$ Model. *Phys. Rev. Lett.* **92**, 146403 (2004).

[8] Mishchenko, A. S. & Nagaosa, N. Electron-Phonon Coupling and a Polaron in the $t-J$ Model: From the Weak to the Strong Coupling Regime. *Phys. Rev. Lett.* **93**, 036402 (2004).

[9] Rösch, O., et al. Polaronic Behavior of Undoped High-T_c Cuprate Superconductors from Angle-Resolved Photoemission Spectra. *Phys. Rev. Lett.* **95**, 227002 (2005).

10

248 [10] Cataudella, V., De Filippis, G., Mishchenko, A. S. & Nagaosa, N. Temperature Dependence
249 of the Angle Resolved Photoemission Spectra in the Undoped Cuprates: Self-Consistent
250 Approach to the $t-J$ Holstein Model. *Phys. Rev. Lett.* **99**, 226402 (2007).
251 [11] De Filippis, G., Cataudella, V., Mishchenko, A. S. & Nagaosa, N. Nonlocal Composite Spin-
252 Lattice Polarons in High Temperature Superconductors. *Phys. Rev. Lett.* **99**, 146405 (2007).
253 [12] De Filippis, G. et al. Quantum Dynamics of the Hubbard-Holstein Model in Equilibrium
254 and Nonequilibrium: Application to Pump-Probe Phenomena. *Phys. Rev. Lett.* **109**, 176402
255 (2012).
256 [13] Novelli, F. et al. Witnessing the formation and relaxation of dressed quasi-particles in a
257 strongly correlated electron system. *Nature Communications* **5**, 5112 (2014).
258 [14] Farina, D. et al. Electron-phonon coupling in the undoped cuprate $YBa_2Cu_3O_6$ estimated
259 from Raman and optical conductivity spectra. *Phys. Rev. B.* **98**, 121104 (2018).
260 [15] Lanzara, A. et al. Evidence for ubiquitous strong electron-phonon coupling in high-
261 temperature superconductors. *Nature* **412**, 510-514 (2001).
262 [16] Johnson, P. D. et al., Doping and Temperature Dependence of the Mass Enhancement Ob-
263 served in the Cuprate $Bi_2Sr_2CaCu_2O_{8+\delta}$. *Phys. Rev. Lett.* **87**, 177007 (2001).
264 [17] Shen K. M. et al., Missing Quasiparticles and the Chemical Potential Puzzle in the Doping
265 Evolution of the Cuprate Superconductors. *Phys. Rev. Lett.* **93**, 267002 (2004).
266 [18] Zhou X. J. et al., Multiple Bosonic Mode Coupling in the Electron Self-Energy of
267 $(La_{2-x}Sr_z)CuO_4$. *Phys. Rev. Lett.* **95**, 117001 (2005).
268 [19] Mishchenko, A. S. et al. Charge Dynamics of Doped Holes in High T_c Cuprate Superconduc-
269 tors: A Clue from Optical Conductivity. *Phys. Rev. Lett.* **100**, 166401 (2008).
270 [20] Carbone, F, Yang, D.-S., Giannini, E., & Zewail, A. H. Direct role of structural dynamics in
271 electron-lattice coupling of superconducting cuprates. *PNAS* **105**, 20161–20166 (2008).
272 [21] Mishchenko, A. S., Nagaosa, M. Shen, N., K., Shen, Z.-X., Zhou, X. J., & Devereaux, T. P.
273 Polaronic metal in lightly doped high-T_c cuprates. *EPL* **95**, 57007 (2011).
274 [22] Migdal, A. B. Interaction between electrons and lattice vibrations in a normal metal. *J. Exptl.
275 Theoret. Phys.* **34** 1438-1446 (1958) [*Sov. Phys. JETP* **7**, 996-1001 (1958)].
276 [23] Husanu, M.-A. et al. Electron-polaron dichotomy of charge carriers in perovskite oxides.
277 *Communications Physics* **3**, 62 (2020).
278 [24] Ummarino, G. A. & Gonnelli, R. S. Breakdown of Migdal's theorem and intensity of electron-
279 phonon coupling in high-T_c superconductors. *Phys. Rev. B* **56**, R14279-R14282 (1997).
280 [25] C. Grimaldi, C., Pietronero, L., & Strassler, S. Nonadiabatic Superconductivity: Electron-
281 Phonon Interaction Beyond Migdal's Theorem. *Phys. Rev. Lett.* **75**, 1158-1161 (1995).
282 [26] Schrodi, F., Oppeneer P. M., & Aperis, A. Full-bandwidth Eliashberg theory of superconduc-
283 tivity beyond Migdal's approximation. *Phys. Rev. B* **102**, 024503 (2020).
284 [27] Prokof'ev, N. V. & Svistunov, B. V. Polaron Problem by Diagrammatic Quantum Monte
285 Carlo. *Phys. Rev. Lett.* **81**, 2514-2517 (1998).
286 [28] Mishchenko, A. S., Prokof'ev, N. V., Sakamoto, A. & Svistunov, B. V. Diagrammatic quan-
287 tum Monte Carlo study of the Fröhlich polaron. *Phys. Rev. B* **62**, 6317-6336 (2000).
288 [29] Mishchenko, A. S., Nagaosa, N. & Prokof'ev, N. Diagrammatic Monte Carlo Method for
289 Many-Polaron Problems. *Phys. Rev. Lett.* **113**, 166402 (2014).
290 [30] Macridin, A., Sawatzky, G. A. & Jarrell, M. Two-dimensional Hubbard-Holstein bipolaron.
291 *Phys. Rev. B* **69**, 245111 (2004).
292 [31] Kane, C. L., Lee, P. A. & Read, N. Motion of a single hole in a quantum antiferromagnet.
293 *Phys. Rev. B* **39**, 6880-6897 (1989).
294 [32] Dagotto, E. Correlated electrons in high-temperature superconductors. *Rev. Mod. Phys.* **66**,
295 763-840 (1994).
296 [33] Blankenbecler, R., Scalapino, D. J. & Sugar, R. L. Monte Carlo calculations of coupled
297 boson-fermion systems. I. *Phys. Rev. D* **24**, 2278-2286 (1981).
298 [34] White, S. R., Scalapino, D. J., Sugar R. L., Loh E. Y., Gubernatis J. E., & Scalettar R. T.
299 Numerical study of the two-dimensional Hubbard model. *Phys. Rev. B* **40**, 506 (1989).
300 [35] Noack, R. M. & Scalapino, D. J. Green's-function self-energies in the two-dimensional Holstein
301 model. *Phys. Rev. B* **47**, 305-308 (1993).
302 [36] Georges, A., Kotliar, G., Krauth, W. & Rozenberg, M. J. Dynamical mean-field theory of
303 strongly correlated fermion systems and the limit of infinite dimensions. *Rev. Mod. Phys.* **86**,
304 13-125 (1996).

[37] Bauer, J., Han, J. E. & Gunnarsson, O. Quantitative reliability study of the Migdal-Eliashberg theory for strong electron-phonon coupling in superconductors. *Phys. Rev. B* **84**, 184531 (2011).

[38] Brovnman, E. G. & Kagan, Yu. The Phonon Spectrum of Metals. *J. Exptl. Theoret. Phys.* **52** 557-574 (1967) [*Sov. Phys. JETP* **25**, 365-376 (1967)].

[39] Tupitsyn, I. S., Mishchenko, A. S., Nagaosa, N. & Prokof'ev, N. Coulomb and electron-phonon interactions in metals. *Phys. Rev. B* **94**, 155145 (2016).

[40] See supplemental material.

[41] Goulko, O., Mishchenko, A. S., Pollet, L., Prokof'ev, N. & Svistunov, B. Numerical analytic continuation: Answers to well-posed questions. *Phys. Rev. B* **95**, 014102 (2017).

[42] Krsnik, J., Strocov, V. N., Nagaosa, N., Barišić, O. S., Rukelj, Z., Yakubenya, S. M., & Mishchenko, A. S. Manifestations of the electron-phonon interaction range in angle-resolved photoemission spectra. *Phys. Rev. B* **102**, 121108(R) (2020).

[43] Devereaux, T. P., Cuk, T., Shen, Z.-X. & Nagaosa, N. Anisotropic Electron-Phonon Interaction in the Cuprates. *Phys. Rev. Lett.* **93**, 117004 (2004).

[44] Veenstra, C. N., Goodvin, G. L., Berciu, M. & Damascelli, A. Elusive electron-phonon coupling in quantitative analyses of the spectral function. *Phys. Rev. B* **82**, 012504 (2010).

[45] Bonča, J. and Trugman, S. A. & Batistić I. Holstein polaron. *Phys. Rev. B* **60**, 1633-1642 (1999).

[46] Mishchenko, A. S., Nagaosa, N., Prokof'ev, N. V., Sakamoto, A. & Svistunov, B. V. Self-trapping of polarons in the Rashba-Pekar model. *Phys. Rev. B* **66**, 020301 (2002).

[47] Sherman, E. Ya. & Ambrosch-Draxl C. Multiband electron-phonon coupling in the cuprates: Raman scattering and charge fluctuations, *Phys. Rev. B* **62**, 973 (2000).

[48] Johnston S., Vernay, F., Moritz B., Shen, Z.-X., Nagaosa, N., Zaanen J., & Devereaux T. P. Systematic study of electron-phonon coupling to oxygen modes across the cuprates. *Phys. Rev. B* **82**, 064513 (2010).

[49] Dahm, T., Hinkov, V., Borisenko, S. V., Kordyuk, A. A., Zabolotnyy, V. B., Fink, J., Buchner, B., Scalapino, D. J., Hanke, W. & Keimer, B. Strength of the spin-fluctuation-mediated pairing interaction in a high-temperature superconductor. Nature Phys., **5**, 217-221 (2009).

[50] Anzai, H., Arita, M., Namatame, H., Taniguchi, M., Ishikado, M., Fujita, K., Ishida, S., Uchida, S. & Ino, A. A New Landscape of Multiple Dispersion Kinks in a High-T_c Cuprate Superconductor. Sci. Rep. **7**, 4830 (2017).

8. Acknowledgements

9. Author contributions

A.S.M., I.S.T., and N.P. developed Diagrammatic Monte Carlo codes. A.S.M. and N.N. conceived the idea of calculations. A.S.M. performed calculations and wrote the manuscript. All authors discussed the results, interpretations, and scientific concepts.

10. Competing interests

The authors declare no competing interests.

11. Additional information

Supplementary information is available for this paper at https://?????

Correspondence and requests for materials should be addressed to A.S.M.
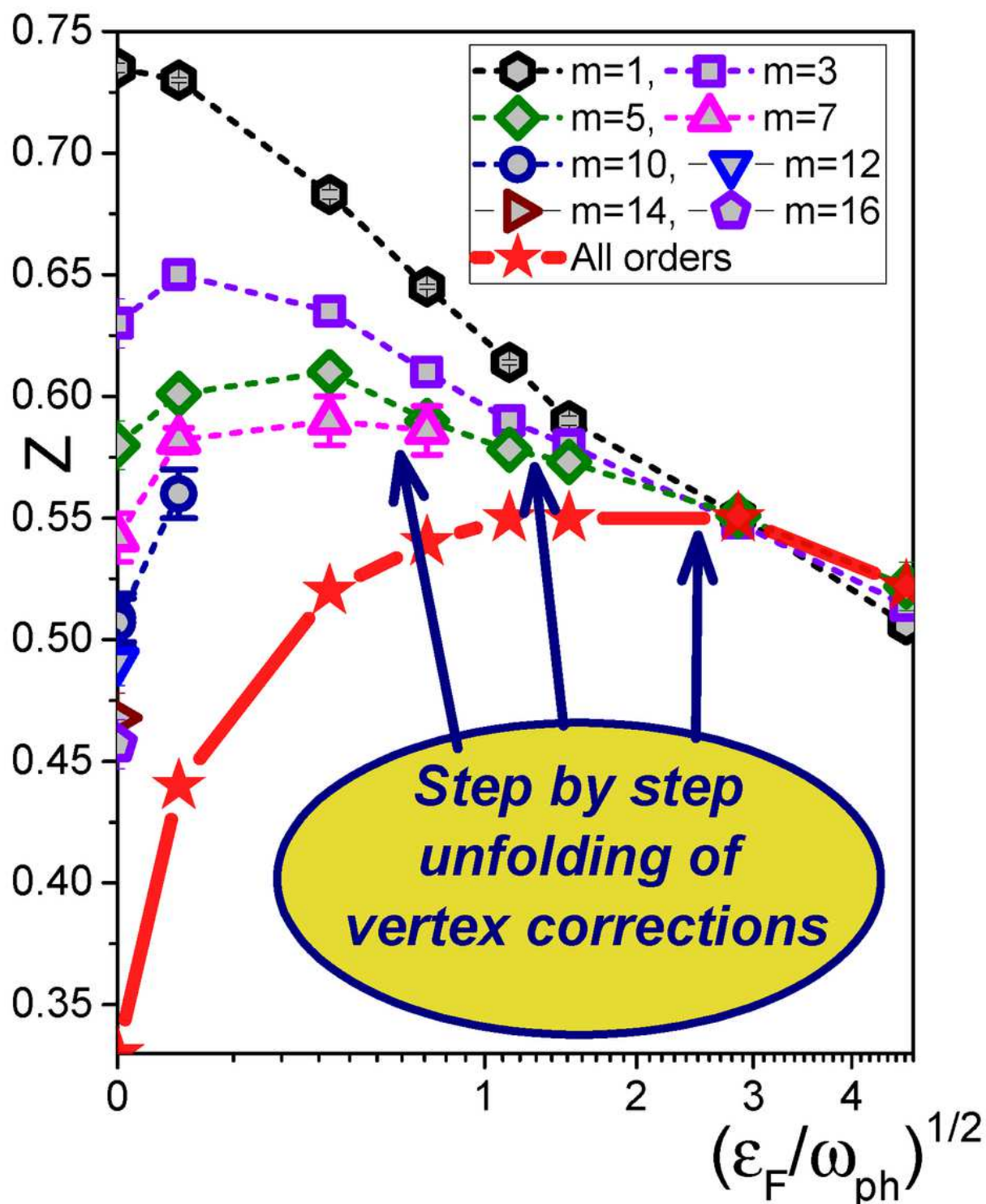
Figures

Figure 1

Quasi-particle residue at the Fermi (FS) as a function of ratio between the Fermi energy and phonon frequency without (m = 1) and with vertex corrections (m > 1). Symbols and dashed lines represent data obtained by skeleton expansions truncated at some finite order m. The solid red line with stars is

obtained by extrapolation to the infinite diagram-order limit m ⟶ ∞. The error bars, if not visible, are smaller than the symbol sizes.
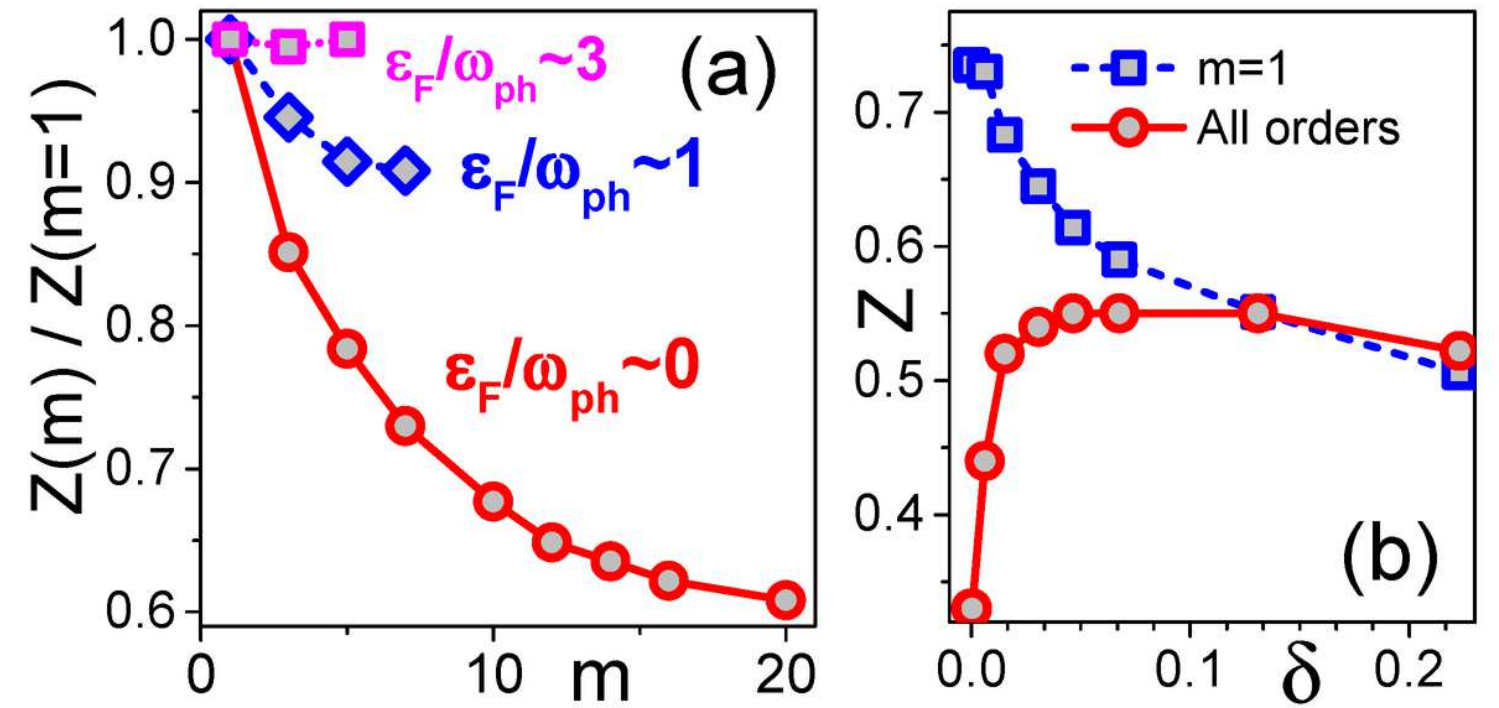

Figure 2

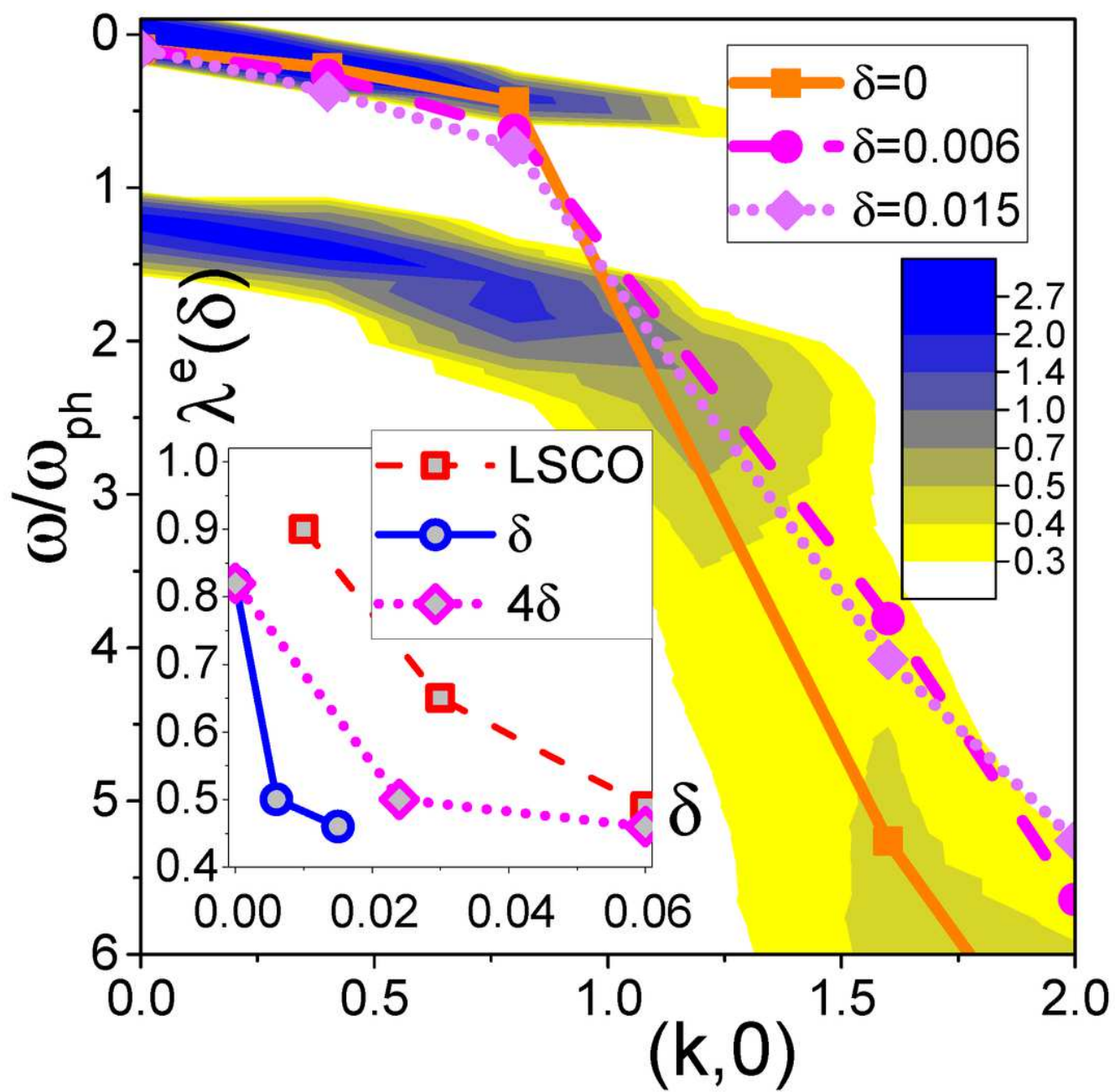Please see the Manuscript PDF file for the complete figure caption.

Figure 3

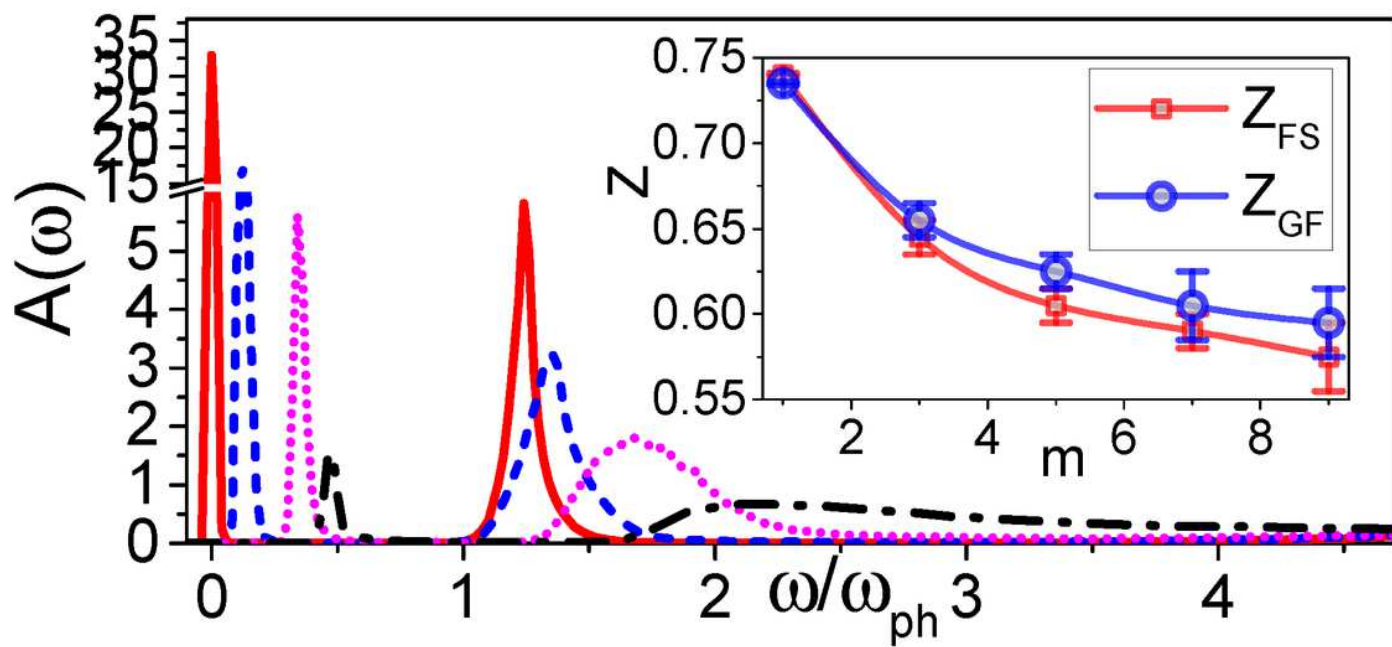Please see the Manuscript PDF file for the complete figure caption.

Figure 4

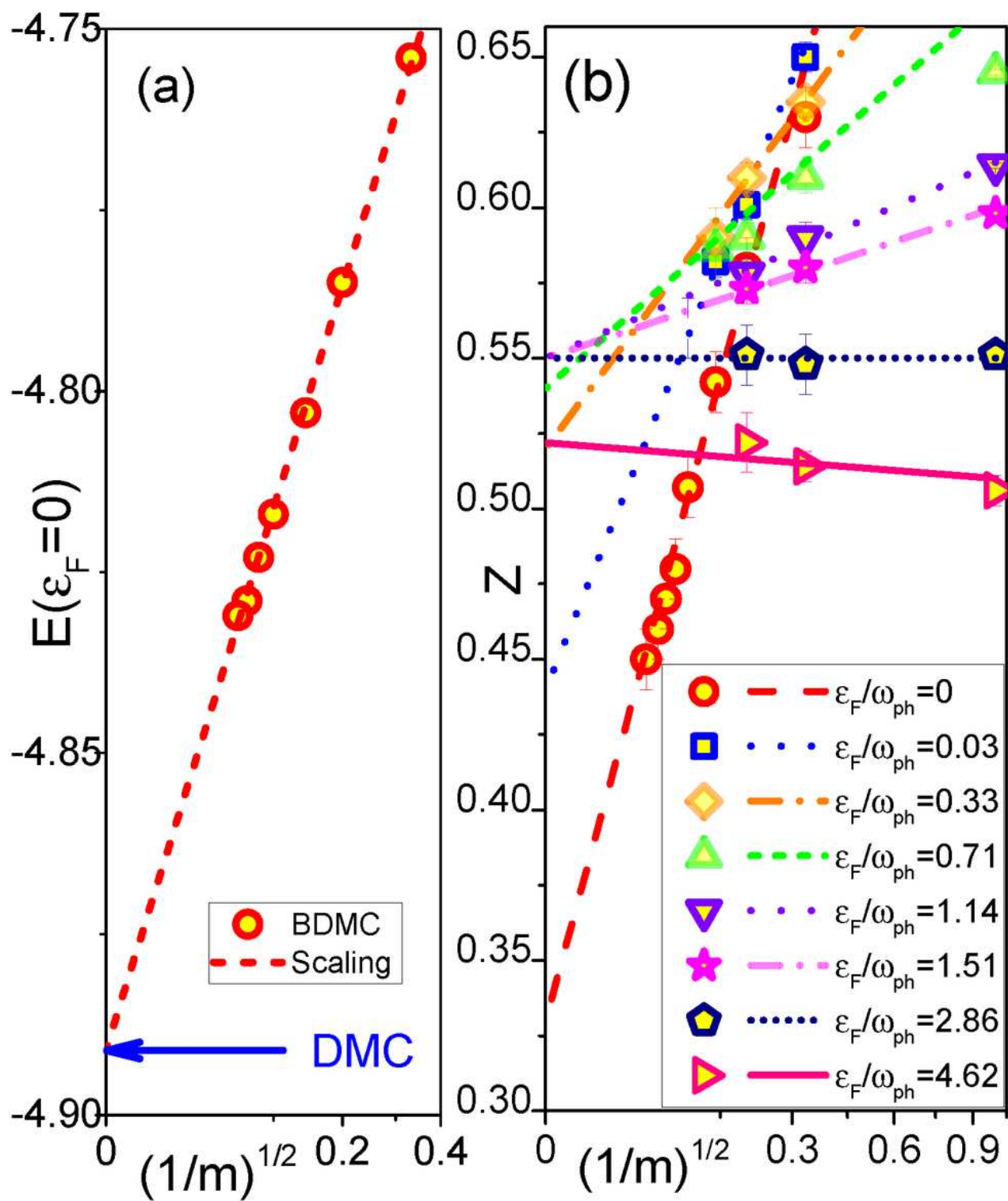Please see the Manuscript PDF file for the complete figure caption.

Figure 5

Please see the Manuscript PDF file for the complete figure caption.

Supplementary Files

This is a list of supplementary files associated with this preprint. Click to download.

- supplement05.pdf